Thermodynamic, thermoelectric, and magnetic properties of $FeSb_2$: A combined first-principles and experimental study

M. S. Diakhate,[1,*] R. P. Hermann,[1,2] A. Möchel,[1,2] I. Sergueev,[3] M. Søndergaard,[4] M. Christensen,[5] and M. J. Verstraete[1]

[1]*Faculté des Sciences, Université de Liège, B-4000 Liège, Belgium*

[2]*Jülich Centre for Neutron Science, JCNS and Peter Grünberg Institut PGI, JARA-FIT, Forschungszentrum Jülich GmbH, D-52425 Jülich, Germany.*

[3]*European Synchrotron Radiation Facility, F-38043 Grenoble cedex, France*

[4]*Center for Energy Materials & iNANO, Department of Chemistry, Aarhus University, DK-8000 Aarhus C. Denmark*

[5]*Center for Materials Crystallography & iNANO, Department of Chemistry, Aarhus University, DK-8000 Aarhus C. Denmark*

(Received 9 May 2011; published 29 September 2011)

We analyze the thermodynamic, magnetic, and transport properties of the narrow band-gap semiconductor $FeSb_2$ using density functional theory calculations corroborated by nuclear inelastic spectroscopy and ultrasound experiments. The vibrational properties (phonon spectrum, density of states, heat capacity) and elastic constants are computed through response function calculations and are in good agreements with the measurements. The electron-phonon coupling effects are also studied. The estimations of linewidth broadening due to electron-phonon coupling along the high-symmetry directions in the first Brillouin zone are given. The linewidth broadening reaches the largest value for Fe optical modes in the vicinity of the $X[0.5,0,0]$ point. The broadening, when compared to those obtained at the other symmetry points, differs by up to two orders of magnitude. From the Boltzmann theory applied to our electronic band structure, we investigate the electrical transport properties. It is found that a purely electronic structure description is incompatible with the record value of the Seebeck coefficient experimentally observed at $T \approx 12$ K. The diamagnetic to paramagnetic crossover at a temperature around 100 K is also described from the calculation of the magnetic susceptibility, and results compare well with experiment.

DOI: 10.1103/PhysRevB.84.125210 PACS number(s): 63.20.dk, 71.38.−k, 63.20.dd

I. INTRODUCTION

The study of the thermodynamic, thermoelectric, and magnetic properties of iron diantimonide $FeSb_2$ has been the subject of intense research investigations.[1–4] The particular interest in this material is due to its interesting low-temperature physical properties and the considerable potential applications, the most promising of which is in the development of cryorefrigeration because of its large thermoelectric power at low temperature.[4]

$FeSb_2$ crystallizes in the loellingite (orthorhombic marcasite type) structure with Fe ions surrounded by deformed Sb octahedra[5] and contains two formula units per unit cell. The low-temperature state is a semiconductor with an extremely narrow indirect band gap, which promotes strong correlation effects between d and conduction-band states.[6–9] The minimum direct gap value extracted from reflectivity measurements[10,11] ranges between 30 and 40 meV. Recent band-structure calculations[12] have shown that it is possible to properly describe the indirect semiconducting gap of $FeSb_2$ by going beyond standard density functional theory (DFT) methods for instance using GW calculations.

The physical properties of $FeSb_2$ are similar in many respects to those of iron silicide FeSi.[13,14] The most remarkable observed similarities are the temperature-dependent magnetic susceptibility[15,16] $\chi(T)$ and the strong anisotropic electrical transport properties.[17–19] For a magnetic field applied along the c axis, the system evolves from a diamagnetic state toward a paramagnetic state through a crossover temperature at about 100 K. The electrical resistivity exhibits a semiconducting behavior along the a and c axes, whereas, for the b axis, a semiconducting-metallic crossover temperature of 40 K is observed. Among the open questions regarding the temperature dependence of the physical properties of $FeSb_2$, most attention has recently been focused on the origin of the huge low-temperature thermopower. Of particular interest is the issue of whether the thermopower is purely electronic, as is usually assumed, or if there are some other important effects due to phonon drag,[20] for instance. The physical origin of this phenomenon is in fact not yet clarified. Adding to properties observed earlier, Bentien *et al.*[21] recently found that $FeSb_2$ exhibits a record Seebeck coefficient $S \approx -45\,000\ \mu V\ K^{-1}$ at $T \approx 12$ K, and the thermoelectric power factor $PF = S^2\rho^{-1}$, where ρ represents the electrical resistivity, can reach a value of $\approx 2300\ \mu WK^{-2}\ cm^{-1}$. This value is 65 times larger than the reference value measured for Bi_2Te_3-based thermoelectric materials. However, the figure of merit $ZT = S^2\rho^{-1}\kappa^{-1}T$ is rather low, due to the large value of the thermal conductivity[12] $\kappa = 250\ WK^{-1}m^{-1}$ at $T \approx 12$ K.

Herein, we combine experimental and theoretical investigation of transport, magnetic, and vibrational properties of $FeSb_2$. We analyze the transport coefficients within an electronic-structure picture where the contribution of the lattice thermal conductivity κ_L to ZT is neglected (low-temperature approximation). Because the electrical transport properties of narrow band-gap semiconductors are very sensitive to chemical substitution,[22] we have investigated the effect of donor impurity doping on the Seebeck coefficient. The exponentially activated paramagnetic susceptibility[23] with increasing temperature is highlighted. Regarding the vibrational properties, few studies have been performed so far,[24,25] and the results were presented from the point of view of its absorption

spectrum in comparison with those obtained in FeSi, which has similar physical properties.[10,18] This restriction does not allow a more detailed description of some physical properties, such as the lattice vibrations and their interaction with electrons, which are necessary to understand the mechanism governing the low-temperature thermoelectric power of $FeSb_2$. The experimental phonon density of states, sound velocities, and shear modulus were obtained by nuclear inelastic scattering and resonant ultrasound spectroscopy measurements. Results are presented in comparison with those calculated using methods based on response function calculations.[26]

II. METHODS

A. Computational methods

The calculations were carried out using the density functional theory[27,28] and norm-conserving pseudopotentials (including spin-orbit corrections[29] for Sb) in the generalized gradient (GGA) approximation as implemented in the ABINIT package.[30] Details of our calculation are as follows. The exchange-correlation potential is in the form of Perdew-Burke-Ernzerhof (PBE).[31] We use a plane-wave basis set with a kinetic energy cutoff of 45 Ha. For the atomic positions relaxation, we sample the entire Brillouin zone (BZ) with $16 \times 16 \times 16$ k points corresponding to 2097 k points in the irreducible Brillouin zone (IBZ). The BZ integrations were performed using a Gaussian smearing method with a width of 2.7 meV. The total energy is converged to within 3×10^{-4} meV and the obtained equilibrium structure is of loellingite type, with an orthorhombic cell. The calculated lattice parameters are $a = 5.83$ Å, $b = 6.50$ Å, and $c = 3.16$ Å. These results are consistent with experimental values.[3] In order to compute the transport properties and electron-phonon interaction properties, we need a finer k-point grid. The electronic eigenvalues and phonon eigenfrequencies were determined on a grid consisting of $24 \times 24 \times 24$ k vectors and $4 \times 4 \times 4$ phonon wave vectors. The phonon density of states and dispersion along high-symmetry lines have been obtained by standard methods based on response function calculations.[26] We considered perturbations in the high-symmetry directions of the crystallographic cell. The resulting thermodynamic properties (the vibrational entropy and heat capacity) were calculated using quasiharmonic approximation.[32,33] The calculation of transport properties was performed using a denser mesh of 450 000 k points of the BZ. The semiclassical Boltzmann theory as implemented in the transport code BOLTZTRAP (Ref. 34) has been used to compute the electrical transport coefficients and the magnetic susceptibility. We point out that there is no alternative magnetic solution for the ground state of $FeSb_2$, in agreement with experiment.[17]

B. Experimental methods

The sample enriched with ^{57}Fe was made from finely ground powder of pure elements. The powders were mixed thoroughly before they were placed in a corundum crucible and sealed in vacuum in a quartz tube. The elements were allowed to react for 1 week at 730 °C. The sample was pure with the measured resolution obtained by a Bruker D8 Advanced equipped with $CuK_{\bar{\alpha}}1$ and an energy dispersive Sol-X detector. The sample for the resonance ultrasound spectroscopy was a nonenriched sample prepared in a similar way followed by spark plasma sintering pressing. A pellet was pressed by heating to 600 °C in 5 min at 60 MPa and held at 600 °C for 10 min. Before pressing a small impurity of Sb was observed by x-ray diffraction, after pressing a tiny amount of Fe was observed, however the content was too small for quantitative refinements.

The partial density of phonon states (DPS) of Sb and Fe were obtained by nuclear inelastic scattering (NIS) measurements. The technique and the extraction of the DPS from the NIS spectra are explained in Refs. 35–37. The measurements with the ^{57}Fe and the ^{121}Sb resonance took place on the 95% ^{57}Fe enriched powder sample at the ESRF ID18 and ID22N beamlines, respectively, in 16 bunch mode, and at 50 and 67 K, respectively, in order to reduce the multiphonon contributions. The resolution was 0.7 and 1.3 meV full width at half maximum (FWHM) for measurements with the ^{57}Fe and ^{121}Sb resonance, respectively.

The resonant ultrasound spectroscopy (RUS) response was measured with a homemade inset for a QD-PPMS. The measurements were done on a polished $2.205(2) \times 2.118(2) \times 1.784(2)$ mm^3 polycrystalline sintered powder sample upon cooling between 300 and 10 K. It was verified by Laue diffraction that the sample is polycrystalline. The density of the sample was ∼98% of the x-ray density. Only 20 resonance frequencies could be reliably determined and modeled using a finite element algorithm for a rectangular parallelepiped with a 10th-order polynomial fit for the displacements.[38] The root-mean-square deviation of the fits was of ∼0.8%, i.e., somewhat large. A too small number of resonance lines had a significant c_{11} contribution, thus, it can not be reliably determined. The temperature dependence of the c_{44} component was obtained through fits and then verified by the temperature variation of particular resonance frequencies, which depend by more than 95% on c_{44}. The weakness in the modeling likely comes from texture in the sample caused by the sintering process.

III. RESULTS AND DISCUSSIONS

A. Electronic band structure

The GGA electronic band structure is displayed in Fig. 1. The maximum of the valence band is at the R[0.5,0.5,0.5] point and the minimum of the conduction band is found in the line between the points Γ and Z[0 0 0.5]. The semiconducting optical gap was estimated at 35 meV from reflectivity measurements;[10] this is consistent with the calculated direct gap of 33 meV, despite the well-known underestimation of the band gap within DFT (see right inset to Fig. 1). The density of states in the vicinity of the Fermi level is largely dominated by the Fe-d states, however, a substantial contribution from the Sb-p states is observed. The projected DOS show that the two major peaks at the top of the valence band and the bottom of the conduction band have mainly d_{z^2} and $d_{x^2-y^2}$ characters.[4] These two enhanced narrow bands and the small band gap suggest strong electronic correlation effects that may be responsible for the magnetic and transport anomalies in $FeSb_2$ at low temperature.

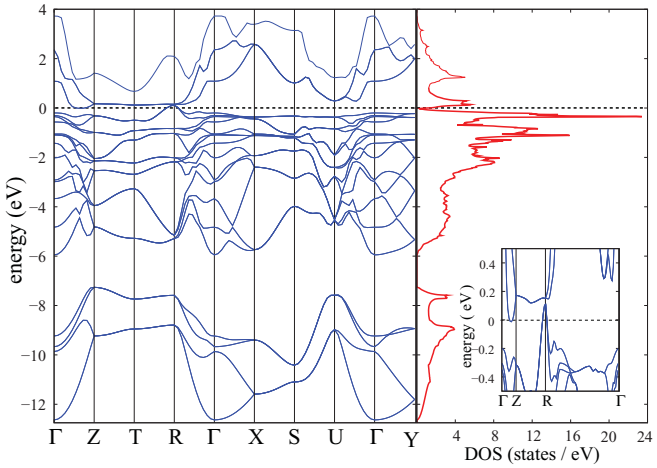

FIG. 1. (Color online) Calculated electronic band structure and density of states of $FeSb_2$ using GGA. The red dotted line indicates the Fermi level. The inset right figure shows the small direct band gap at the R [0.5,0.5,0.5] point (corner of the first Brillouin zone), and the overlap between the maximum of the valence band, which is located at R point and the minimum of the conduction band lying between the Γ and Z [0 0 0.5] points.

B. Magnetic susceptibility

The study of the magnetic susceptibility reveals an interesting diamagnetic to paramagnetic transition at temperature around 100 K, as experimentally observed.[23] Figure 2 displays the magnetic susceptibility χ as a function of temperature. The magnetic susceptibility is calculated from the electronic density of states $g(\epsilon)$ (Fig. 1, right panel) and the derivative of the Fermi distribution function $f(\epsilon,\mu,T_e)$ with respect to energy

$$\chi = -2\mu_o\mu_B^2 \int g(\epsilon)[\partial f(\epsilon,\mu,T_e)/\partial\epsilon]d\epsilon + \chi_0, \qquad (1)$$

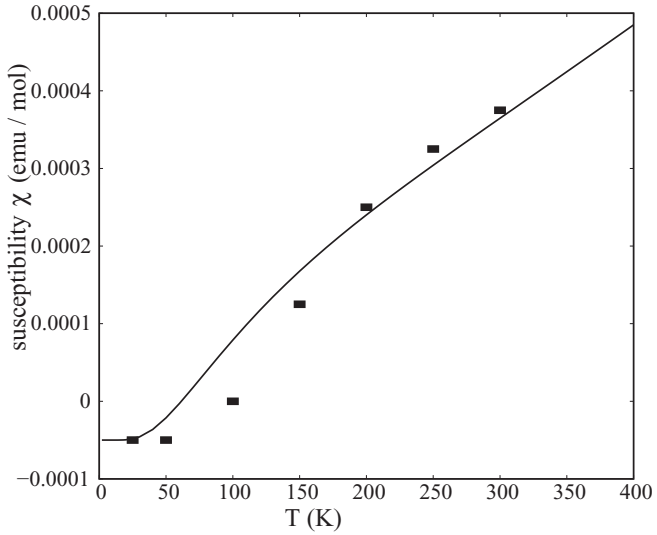

FIG. 2. The temperature evolution of the magnetic susceptibility compared with experimental results extracted from Ref. 3. χ evolves from a constant value $= -4.510^{-5}$ emu/mol at low temperatures (diamagnetic region) toward positive values (paramagnetic region) above $T = 80$ K.

where μ_o and μ_B are the magnetic permittivity of vacuum and the Bohr magneton, respectively. The calculation of the derivative $\partial f(\epsilon,\mu,T_e)/\partial\epsilon$ requires the knowledge of the chemical potential μ as a function of electronic temperature, which is evaluated from the conservation of total electrons number $N_e = \int g(\epsilon)f(\epsilon,\mu,T_e)$. $\chi_0 = -4.510^{-5}$ emu/mol is an additional constant term due to the core diamagnetism.[3] Below 40 K, χ is temperature independent. The diamagnetism ($\chi < 0$) is progressively reduced with rising temperature leading to the paramagnetic behavior above 80 K ($\chi > 0$). The small crossover temperature $T \approx 80$ K is attributed to the narrow band gap. $FeSb_2$ can be presented as a Kondo insulator system where the electronic structure is characterized by two dominant bands at the vicinity of the Fermi level (see Fig. 1), with a given width of W, separated by a gap. Raising the temperature leads to delocalization of electrons from lower bands to upper bands and activates the Pauli magnetic susceptibility[3] as shown in Fig. 2. The same scenario has been found to be the underlying mechanism of phase changes observed in the related system FeSi.[10]

C. Transport properties

As previously mentioned, the calculation of transport coefficients was performed by using the semiclassical Boltzmann theory applied to the GGA electronic band structure described in Sec. III A.

1. Seebeck coefficient

Figure 3 shows the Seebeck coefficient S as function of temperature. A spectacular drop is observed at low temperatures, yielding a minimum value of $S_{\max} \approx -800$ μV K^{-1} at $T \approx 15$ K. The enhanced peak is followed by a rapid increase of S with T toward positive values above $T \approx 25$ K. Whereas a fairly good agreement is obtained with experimental results,[39] $S_{\max}$ is rather different from the record value $S_{\max} \approx -45\,000$ μV K^{-1} measured by Bentien *et al.*[21] along the c direction. Our calculations also show that S is relatively

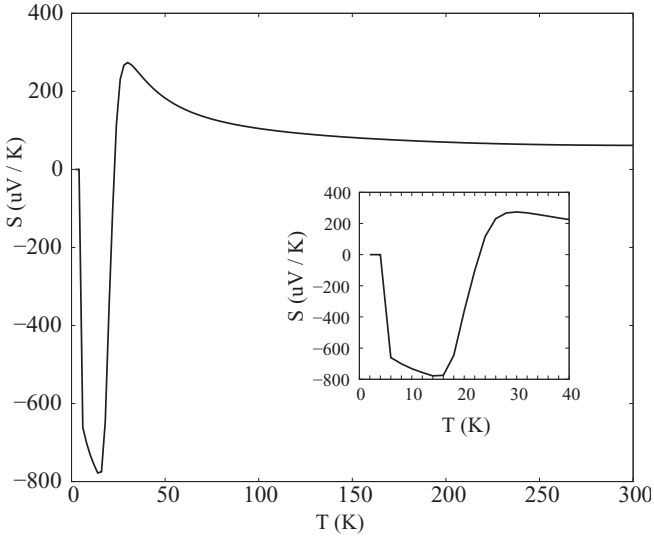

FIG. 3. Seebeck coefficient S vs temperature T. The inset shows the low-temperature curve between 0 and 40 K for S.

larger in the c than in the a or b directions. The directional dependence of S is not given here.

However, the observed record value of $S(T)$ can not be quantitatively reproduced by a purely electronic-structure picture, or by a classical description of electron diffusion in a nondegenerate system.[40] This implies that other contributions must be present. Although many aspects may suggest that the phonon drag effect[20] plays a dominant role in the large enhancement of S at $T \approx 12$ K, it was also shown in a comparative study[40] on related systems such as $RuSb_2$ that the role of phonon drag is minor.

2. Donor doping

The quality of the sample used for experimental measurements is known to have a large influence on the value of S_{max}. The measured values of S_{max} depend on the purity of the polycrystal; similar measurements[4] with a less pure polycrystal have led to much smaller values.

Our observations indicate that S is very sensitive to the value of the chemical potential μ as is shown in Fig. 4. The value of μ depends on the concentration of charge carriers and hence on the purity of the material. In the intrinsic case, where the number of electrons excited to the conduction band n is equal to the number of holes p, left behind, the chemical potential is $\mu \approx \Delta/2 + (3/4)k_B\ Tln(m_h/m_e)$, where m_h and m_e are, respectively, the effective masses of holes and electrons. In this regime, μ is displaced from the middle of the band gap by a term that depends on temperature and the ratio of the effective masses. The point of charge neutrality at $T = 0$ K is very close to the midgap point. For nonzero temperatures, the donor and acceptor sites can be thermally ionized. In the extrinsic case for finite dopings, the charge neutrality condition $n + N_a^- = p + N_d^+$ governs the carrier concentration, where $N_a^- = N_a[1 - f(\Delta - E_a)]$ and $N_d^+ = N_d[1 - f(\Delta - E_d)]$ are the concentration of ionized acceptors and donors. N_a and N_d are the number of acceptors and donors, E_a and E_d the corresponding energy levels, and f the Fermi function.

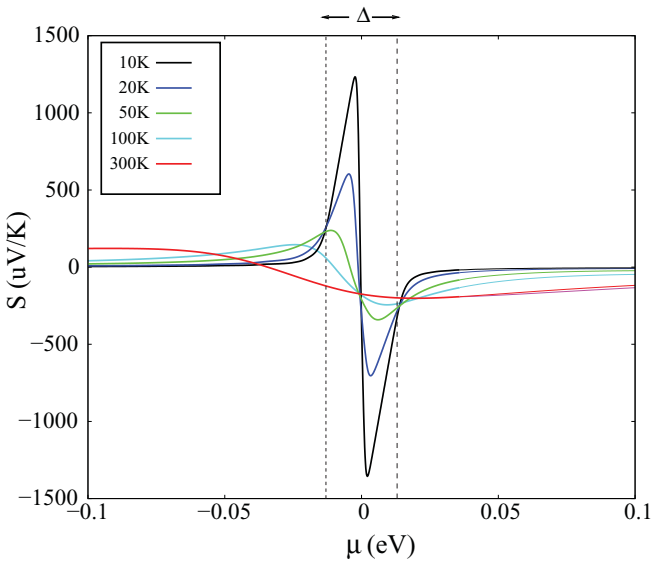

FIG. 4. (Color online) Seebeck coefficient S vs chemical potential μ at different temperatures. S is very sensitive to small changes in μ.

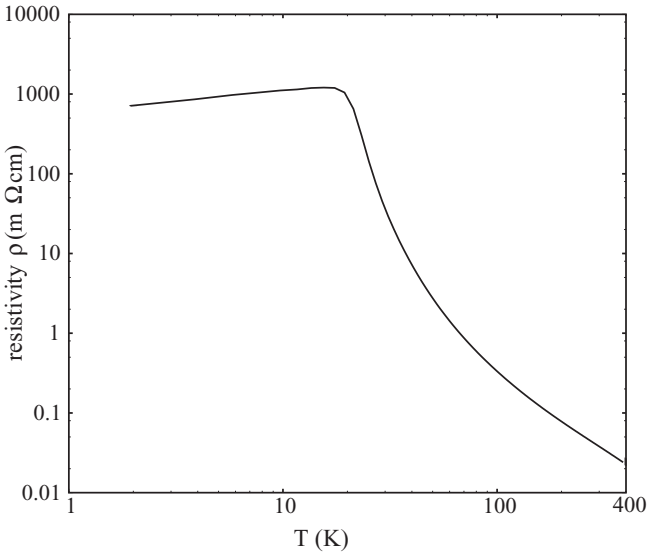

FIG. 5. Calculated electrical resistivity ρ vs temperature in a logarithmic scale. $\rho(T)$ is computed using a constant relaxation time $\tau = 0.225$ ps for the whole temperature range.

In the presence of donor impurities, $n = p + N_d^+$ corresponding to $\mu > 0$ and $S < 0$ in Fig. 4, the chemical potential is $\mu = (\Delta/2 - E^{imp}/2) - k_B\ Tln(n/N_d^+)$, where $E^{imp} = \Delta/2 - E_d$ is the impurity activation energy. The enhancement of the Seebeck coefficient at a given temperature depends on whether the additional carriers bring μ toward its optimal value μ_{opt} or not. We found $\mu_{opt} = 0.21$ meV for $T = 16$ K corresponding to a carrier density of $n = 3.2 \times 10^{15}/cm^3$. This optimum chemical potential, which maximizes S, is located above the midgap point. The optimum carrier density

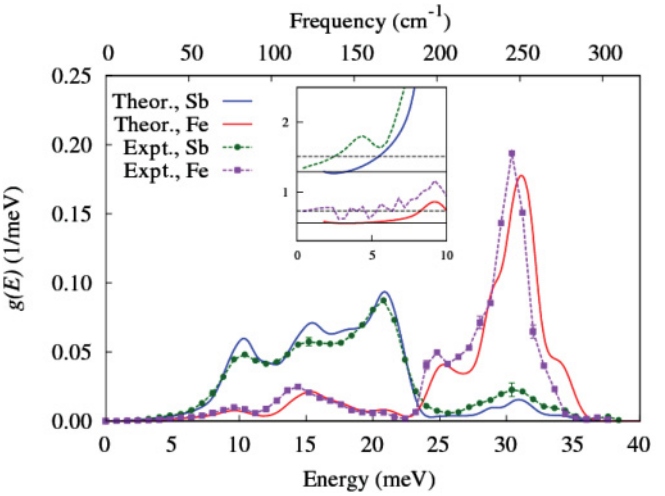

FIG. 6. (Color online) Comparison of the DPS obtained by calculation (Theor.) and by NIS (Expt.) measured with the ^{57}Fe resonance at 50 K and with the ^{121}Sb resonance at 67 K. In the inset, the reduced partial DPS, $g(E)/(E^2)$, is shown in units of $10^{-4}/meV^3$ with the low-energy fit, between 0 and 4 meV, for the Debye levels indicated by the same line style. The Debye level is proportional to the mass of the element and hence different for Fe and Sb.

TABLE I. The thermodynamic properties obtained from the partial DPS at $T = 50$ K.

	Theor.		Expt.	
	Fe	Sb	Fe	Sb
v_s (m/s)	3300(50)	3250(50)	3050(50)	3000(100)
F^m (N/m)	175(5)	150(5)	163(5)	165(5)
θ_D (K)	447(5)	276(5)	405(5)	270(10)

found in Ref. 12 corresponds to $n = 1.3 \times 10^{16}/\text{cm}^3$ at $T = 220$ K. It appears, therefore, that the combination of an optimal doping and small resistivity allows us to maximize the thermopower S.

3. Resistivity

Figure 5 shows the variation of the electrical resistivity ρ with temperature. $\rho(T)$ is evaluated assuming a temperature-independent relaxation time τ of electrons. For the estimation of τ, we fit the experimental data reported in Fig. 2 of Ref. 40 by adjusting the value of ρ at low temperature. We find $\tau = 0.225$ ps. A step further toward a complete theoretical description of the transport properties is to go beyond the constant relaxation-time approximation by taking into account the anisotropic nature of the electron scattering by phonons and the temperature dependence of τ.

Below $T = 400$ K, the resistivity exhibits a semiconducting behavior with two different regions separated by a plateau at $T \approx 20$ K and is similar to what is observed in Refs. 4 and 21. The activation energy above 50 K obtained by fitting the Arrhenius equation $\rho(T) = \rho_0 \exp(E_a/2k_B\ T)$ is estimated to $E_A \sim 350$–450 K in agreement with experimental measurements.[40] Furthermore, it appears from our calculations that the low-temperature resistivity is highly anisotropic. Along the c axis, we observe a large increase of $\rho(T)$ values, in agreement with experimental measurements.[17]

The efficiency of thermoelectric materials is determined by the value of the figure of merit ZT defined above. The reference value measured for Bi_2Te_3-based thermoelectric material is $ZT = 0.9$.[41] A target value larger than 2 is desirable for a large-scale applications. From the definition of ZT, it clearly appears that systems with large thermoelectric power must be both good electrical conductor and very limited in terms of heat conduction, to have a maximum ZT. It is therefore necessary to find a way to separate the electrical and thermal properties in order to maximize ZT, i.e., to obtain high values of the Seebeck coefficient S and low value of the electrical resistivity ρ while minimizing the lattice thermal conductivity κ.

TABLE II. The transverse, longitudinal, and average sound velocities in m/s.

Direction	TA1	TA2	LA	Average v_s
[100]	3181	3649	5123	3703
[010]	2249	3700	5473	2975
[001]	2306	3189	4666	2811
[110]	2754	3108	5285	3243
[011]	2850	3213	4420	3281

D. Phonons and elastic constants

1. Density of states

The calculated partial DPS, $g(E)$, and the DPS obtained from NIS are in good agreement (see Fig. 6). The phonon modes related to Sb are mainly below ~23 meV, whereas the iron modes are in a higher energy range above ~23 meV. There is a small contribution of Sb modes in the high-energy range and of Fe modes in the low-energy range, which is due to the interaction of Sb and Fe modes. The Sb modes have a similar shape than the Sb modes in the skutterudite $FeSb_3$,[37] but the thermodynamic properties, such as the velocity of sound and the Debye temperature in these compounds, are different, as the Fe modes here are in a larger energy range. The experimental Sb phonons are very well reproduced by the calculation. In contrast, for the Fe phonons, although the shape is very well reproduced, the experimental modes are somewhat softer than calculated ones, which might be indicative of some significant softening due do electron-phonon interactions already at 50 K. The Debye level can be obtained from the low-energy range in the reduced DPS, $\lim_{E\to 0}[g(E)/E^2]$ (see inset to Fig. 6). From the Debye level, the velocity of sound v_s can be obtained by $\lim_{E\to 0}[g(E)/E^2] = M_R/(2\pi^2\rho\hbar^3 v_s^3)$, with the mass of the resonant atom M_R and the density of the material ρ. The mean values of v_s obtained from the calculated and experimental Fe DPS are 3300(50) and 3050(50) m/s, respectively, in good agreement with the v_s obtained by the measured Sb DPS (see Table I). The difference between the calculated and experimental velocity of sound can be partly explained by differences in temperature because the experimental DPS was obtained at a finite temperature of 50 K. The partial velocity of sound v_λ along the longitudinal and transversal directions is obtained from the calculated phonon dispersion curves using the acoustic approximation (see Table II). The DPS also gives reliable and direct access to the element-specific mean force constants both for Fe (Ref. 35) and for Sb (Ref. 42) by the relation $F^m = M_R/\hbar \int_0^\infty g(E)E^2 dE$. The obtained F^m values for Fe and Sb from calculation and experiment are in good agreement (see Table I). The element-specific Debye temperatures can be obtained from the DPS with the relation $\theta_D^2 = 3/[k_B{}^2 \int_0^\infty g(E)dE/E^2]$, obtained in the high-temperature limit (see Ref. 35). The obtained calculated and experimental values are in agreement (see Table I).

2. Elastic constants

The polycrystalline average of the c_{44} shear modulus exhibits first softening with increasing temperature up to 120 K, which is the typical behavior observed in most materials (see Fig. 7). However, above 120 K, hardening with increasing temperature is observed, which correlates with the onset of the gradual transition from diamagnetic to paramagnetic behavior and the activation of charge carriers (see experimental data in Fig. 2). This anomalous hardening is a further indication of strong coupling between lattice and electronic degrees of freedom. The qualitative temperature dependence reported herein is not affected by the modeling problems related

TABLE III. Elastic constants of $FeSb_2$ with and without contribution from spin-orbit interaction (SOI) in Voigt notation and in units of GPa.

	Without SOI						With SOI					
α	1	2	3	4	5	6	1	2	3	4	5	6
1	225.8	64.3	72.1				265	68.5	85			
2	64.3	258.1	32.0				68.5	307	49.5			
3	72.1	32.0	186.5				85	49.5	252			
4				45						36		
5					89						70	
6						116						79

to the use of a sintered polycrystalline sample, however, measurements on single crystal will be highly desirable as soon as large enough samples become available in order to quantitatively verify the impact of the coupling of electronic and lattice degrees of freedom on specific elastic moduli.

The elastic constants with and without inclusion of spin-orbit interaction (SOI) were also calculated directly using perturbation theory (wrt strain) as described in Ref. 43. The elastic constant tensor components c_{ij} reported in Table III are for relaxed ions. Note that the tensor was symmetrized. Experimental or other theoretical results are not available for a direct comparison with the calculated elastic constants c_{ij} in Fig. 7. The measurements of c_{44} and the value obtained at low T are consistent with the calculated values (see Table III), but a precise comparison will require measurements on a single crystal. We can also see that the inclusion of effects due to spin-orbit interaction has, as a consequence, to increase the values of all c_{ij}, except for c_{44}, c_{55}, and c_{66} where values are relatively higher in the absence of spin-orbit coupling.

The speeds of sound extracted from the elastic constants are in good agreement with the values reported in Table II, and agree reasonably well with experiments.

3. *Specific heat*

Using the calculated phonon frequencies and density of states, the temperature dependence of specific heat C_v was computed and compared with measurements. The theoretical and experimental results are illustrated in Fig. 8 and are in excellent agreement. The curves evolve smoothly at low temperatures following the Debye model $C_v \sim (\frac{T}{\Theta_D})^3$ and approaches the Dulong-Petit limit $C_v \sim 75$ J mol^{-1} K^{-1} at high temperatures.

E. Electron-phonon coupling

Our results for the phonon dispersion along several symmetry directions together with the corresponding linewidth broadening due to electron-phonon coupling are displayed in Fig. 9. The energy range of phonon modes extending from 0 up to 35 meV as well as the trend of the electron-phonon coupling along the different branches are consistent with a recent direct experimental measurement using inelastic neutron scattering.[44] Among the various areas explored in the first Brillouin zone, we note that the stronger electron-phonon couplings are observed in the vicinity of the Z[0,0,0.5], X[0.5,0,0], and S[0.5,0.5,0] points for the optical modes. As shown in Fig. 6, the optical modes are largely dominated by contribution from Fe ions. The maximum value of the linewidth broadening is achieved at X.

The Eliashberg spectral function $\alpha^2F(\omega)$ is shown in Fig. 10. The value of the dimensionless electron-phonon coupling strength defined through $\lambda = 2\int \alpha^2F(\omega)d\omega/\omega$ is 0.24; this value is fairly low compared to calculated values for simple metals.[45]

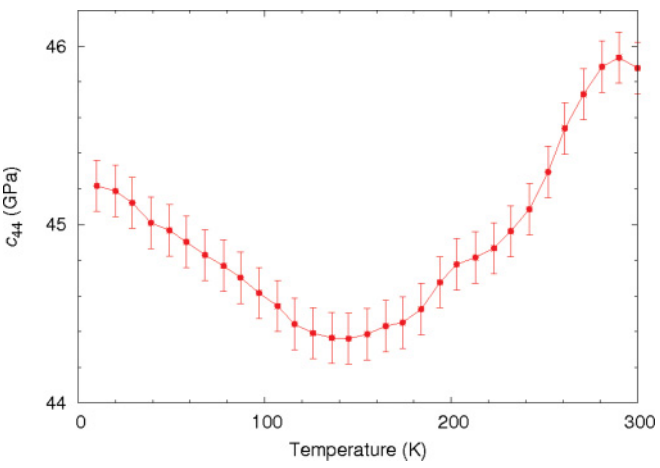

FIG. 7. (Color online) Temperature dependence of the shear modulus c_{44} in a sintered polycrystalline sample of $FeSb_2$.

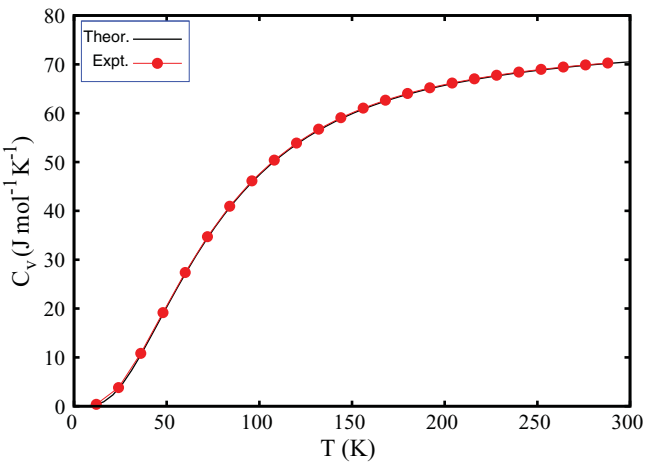

FIG. 8. (Color online) Plot of the specific heat of $FeSb_2$ (full line) as a function of temperature. Results are in very good agreement with measurements (dotted line).

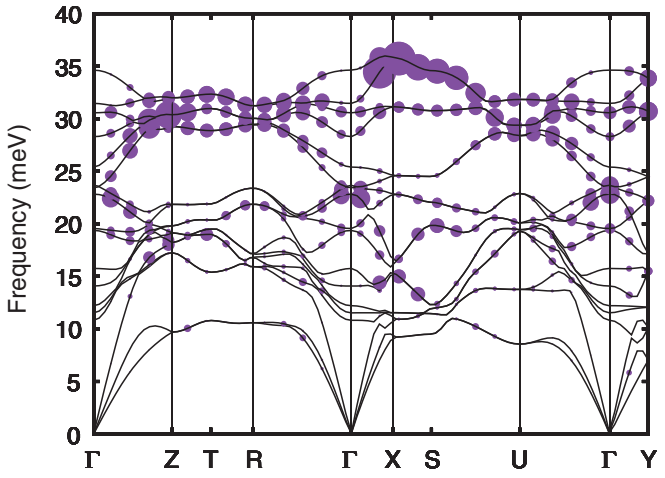

FIG. 9. (Color online) Calculated phonon spectrum of $FeSb_2$ along the high-symmetry lines of the Brillouin zone. The points' size indicates the line broadening due to electron-phonon coupling.

Since no additional broadening due to anharmonic effects can be expected at such low temperatures, our study reveals that the observed electron-phonon interaction may play a major role in the transport properties. This is consistent with recent measurements,[46] which have shown a significant increase of linewidths broadening with temperature in the range 0–40 K.

IV. CONCLUSIONS

We have analyzed the vibrational, thermoelectric, and magnetic properties of the semiconductor $FeSb_2$ through nuclear inelastic scattering, ultrasound experiments, and modeling using DFT. The GGA was sufficient to reliably treat the full set of physical properties on which we focused.

The theoretical approaches provide a valuable insight into the link between the electronic structure and the thermoelectric properties. We have shown that the contribution of the electrons to the thermal conductivity is not the predominant term in the huge negative value of Seebeck coefficient S experimentally observed at low temperature. Our analysis shows that a local electronic-structure picture can explain the position, but not the large amplitude of the $T \sim 12$ K peak in S, suggesting the possible presence of phonon drag effects[20] as it was already found in pure semiconductors silicon[47,48] and germanium.[49,50]

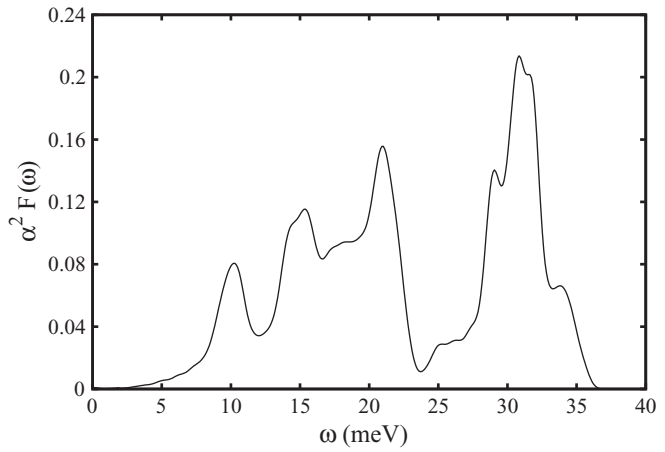

FIG. 10. Electron-phonon spectral function for $FeSb_2$. The results are based on the calculated frequencies.

The correlation between the magnetic susceptibility and the electrical resistivity was highlighted. It can be seen in the behavior of the resistivity when raising temperature. In the low-spin-state diamagnetic phase, the value of the resistivity is four orders of magnitude larger than the value in the paramagnetic high-spin state at room temperature. This significant increase of the electrical conductivity in the paramagnetic region agrees with Goodenough's hypothesis[51] that thermal excitation favors the population of the less localized orbitals rather than more localized orbitals. Therefore, the magnetic susceptibility can be explained either by a low- to high-spin transition or, as mentioned above, by a thermally activated Pauli susceptibility. Further band-structure calculations and experiments are, however, necessary to clarify this issue. For instance, in the band-structure calculation, the orientation of localized and nonlocalized orbitals should be known.

The combined experimental and theoretical study has enabled a direct comparison of measurements and calculations. Although differences were observed between the measured and calculated sound velocities, a very good agreement was obtained for the partial density of phonon states and the temperature dependence of heat capacity. The correlation between the temperature evolution of the shear moduli and the transition from diamagnetic to paramagnetic behavior is emphasized. We have also studied the effects due to electron-phonon coupling. The linewidth broadening along high-symmetry directions was analyzed. The stronger electron-phonon interaction was observed for optical modes of Fe around the Z, X, and S points. This suggests significant mode asymmetry. Since there are no experimental data available yet, our *ab initio* estimations of the linewidth broadening due to electron-phonon interaction presented here may have potential practical implications. They can provide a basis for addressing a detailed experimental study of the effects of electron-phonon coupling in the thermoelectric properties of $FeSb_2$. Inelastic scattering experiments could more deeply investigate this domain, and work is ongoing in this direction. Studies led until now do not reveal a credible and conclusive explanation of the fascinating low-temperature behavior of $FeSb_2$.

ACKNOWLEDGMENTS

The research was funded through the ARC 10/15-03-TheMoTher grant, financed by the French Community of Belgium. We acknowledge ULg-SEGI and the Red Española de Supercomputacion (Cesvima) for supercomputer time. We thank H.-C. Wille and D. Bessas for their support during the NIS measurements and J. Persson for providing the Laue diffractions. The European Synchrotron Radiation Facility is acknowledged for provision of synchrotron radiation beam time at the nuclear resonance station ID18 and D22N. R.H. acknowledges support from the Helmholtz-University Young Investigator Group Lattices Dynamics in Emerging Functional Materials.

*momar.diakhate@ulg.ac.be

[1] R. Hu, V. Mitrovic, and C. Petrovic, Appl. Phys. Lett. **92**, 182108 (2008).

[2] R. Hu, V. F. Mitrović, and C. Petrovic, Phys. Rev. B **76**, 115105 (2007).

[3] C. Petrovic, Y. Lee, T. Vogt, N. D. Lazarov, S. L. Bud'ko, and P. C. Canfield, Phys. Rev. B **72**, 045103 (2005).

[4] A. Bentien, G. K. H. Madsen, S. Johnsen, and B. B. Iversen, Phys. Rev. B **74**, 205105 (2006).

[5] F. Hulliger, Nature (London) **198**, 1081 (1963).

[6] G. Mahan, Solid State Phys. **51**, 81 (1998).

[7] J. K. Freericks, D. O. Demchenko, A. V. Joura, and V. Zlatić, Phys. Rev. B **68**, 195120 (2003).

[8] T. Saso and K. Urasaki, J. Phys. Chem. Solids **63**, 1475 (2002).

[9] C. Grenzebach and G. Czychol, Phys. B (Amsterdam) **359**, 732 (2005).

[10] G. Aeppli and Z. Fisk, Comments Condens. Matter Phys. **16**, 155 (1992).

[11] R. Hu, K. J. Thomas, Y. Lee, T. Vogt, E. S. Choi, V. F. Mitrović, R. P. Hermann, F. Grandjean, P. C. Canfield, J. W. Kim *et al.*, Phys. Rev. B **77**, 085212 (2008).

[12] J. M. Tomczak, K. Haule, T. Miyake, A. Georges, and G. Kotliar, Phys. Rev. B **82**, 085104 (2010).

[13] G. Wertheim, V. Jaccarino, J. Wernick, J. Seitchik, H. Williams, and R. Sherwood, Phys. Lett. **18**, 89 (1965).

[14] V. Jaccarino, G. K. Wertheim, J. H. Wernick, L. R. Walker, and S. Arajs, Phys. Rev. **160**, 476 (1967).

[15] D. Mandrus, J. L. Sarrao, A. Migliori, J. D. Thompson, and Z. Fisk, Phys. Rev. B **51**, 4763 (1995).

[16] Y. Takahashi and T. Moriya, J. Phys. Soc. Jpn. **46**, 1451 (1979).

[17] R. Hu, V. F. Mitrović, and C. Petrovic, Phys. Rev. B **74**, 195130 (2006).

[18] V. I. Anisimov, S. Y. Ezhov, I. S. Elfimov, I. V. Solovyev, and T. M. Rice, Phys. Rev. Lett. **76**, 1735 (1996).

[19] S. Paschen, E. Felder, M. A. Chernikov, L. Degiorgi, H. Schwer, H. R. Ott, D. P. Young, J. L. Sarrao, and Z. Fisk, Phys. Rev. B **56**, 12916 (1997).

[20] C. Herring, Phys. Rev. **96**, 63 (1954).

[21] A. Bentien, S. Johnsen, G. Madsen, B. Iversen, and F. Steglich, Europhys. Lett. **80**, 17008 (2007).

[22] N. Manyala, Y. Sidis, J. Ditusa, G. Aeppli, D. Young, and Z. Fisk, Nat. Matter, Wolfson Coll. Lect. **3**, 255 (2004).

[23] C. Petrovic, J. W. Kim, S. L. Bud'ko, A. I. Goldman, P. C. Canfield, W. Choe, and G. J. Miller, Phys. Rev. B **67**, 155205 (2003).

[24] A. Racu, D. Menzel, J. Schoenes, M. Marutzky, S. Johnsen, and B. Iversen, J. Appl. Phys. **103**, 07C912 (2008).

[25] A. Perucchi, L. Degiorgi, R. Hu, C. Petrovic, and V. F. Mitrovic, Eur. Phys. J. B **54**, 175 (2006).

[26] M. Veithen, X. Gonze, and P. Ghosez, Phys. Rev. B **71**, 125107 (2005).

[27] P. Hohenberg and W. Kohn, Phys. Rev. **136**, 8864 (1964).

[28] W. Kohn and L. Sham, Phys. Rev. **140**, A1133 (1965).

[29] C. Hartwigsen, S. Goedecker, and J. Hutter, Phys. Rev. B **58**, 3641 (1998).

[30] X. Gonze, J.-M. Beuken, R. Caracas, F. Detraux, M. Fuchs, G. M. Rignanese, L. Sindic, M. Verstraete, G. Zerah, F. Jollet *et al.*, Comput. Mater. Sci. **25**, 478 (2002).

[31] J. P. Perdew, K. Burke, and M. Ernzerhof, Phys. Rev. Lett. **77**, 3865 (1996).

[32] F. Bottin, S. Leroux, A. Knyazev, and G. Zerah, Comput. Mater. Sci. **42**, 329 (2008).

[33] A. N. Al-Rawi, A. Kara, P. Staikov, C. Ghosh, and T. S. Rahman, Phys. Rev. Lett. **86**, 2074 (2001).

[34] G. Madsen and D. J. Singh, Comput. Phys. Commun. **175**, 67 (2006).

[35] R. Rüffer and A. Chumakov, Hyperfine Interact. **128**, 225 (2000).

[36] H.-C. Wille, R. P. Hermann, I. Sergueev, O. Leupold, P. van der Linden, B. C. Sales, F. Grandjean, G. J. Long, R. Rüffer, and Y. V. Shvyd'ko, Phys. Rev. B **76**, 140301 (2007).

[37] A. Möchel, I. Sergueev, N. Nguyen, Gary J. Long, F. Grandjean, D. C. Johnson, and R. P. Hermann, Phys. Rev. B **84**, 064302 (2011).

[38] A. Migliori, J. Sarrao, W. M. Visscher, T. Bell, M. Lei, Z. Fisk, and R. Leisure, Physica B (Amsterdam) **183**, 1 (1993).

[39] K. Wang, R. Hu, and C. Petrovic (unpublished).

[40] P. Sun, N. Oeschler, S. Johnsen, B. B. Iversen, and F. Steglich, Phys. Rev. B **79**, 153308 (2009).

[41] G. J. Snyder and E. Toberer, Nature (London) **7**, 105 (2008).

[42] T. Matsunaga *et al.*, Adv. Funct. Mater. **21**, 2232 (2011).

[43] D. R. Hamann, X. Wu, K. M. Rabe, and D. Vanderbilt, Phys. Rev. B **71**, 035117 (2005).

[44] I. A. Zaliznyak, A. T. Savici, V. O. Garlea, R. Hu, and C. Petrovic, Phys. Rev. B **83**, 184414 (2011).

[45] S. Y. Savrasov and D. Y. Savrasov, Phys. Rev. B **54**, 16487 (1996).

[46] N. Lazarević, Z. Popović, R. Hu, and C. Petrovic, Phys. Rev. B **81**, 144302 (2010).

[47] L. Weber, M. Lehr, and E. Gmelin, Phys. Rev. B **46**, 9511 (1992).

[48] L. Weber and E. Gmelin, Appl. Phys. A: Mater. Sci. Process. **53**, 136 (1991).

[49] T. Geballe and G. Hull, Phys. Rev. **94**, 1134 (1954).

[50] A. V. Inyushkin, A. N. Taldenkov, V. I. Ozhogin, K. M. Itoh, and E. E. Haller, Phys. Rev. B **68**, 153203 (2003).

[51] J. Goodenouph, J. Solid State Chem. **1**, 349 (1970).